Eur. Phys. J. Spec. Top.
https://doi.org/10.1140/epjs/s11734-021-00342-3

THE EUROPEAN PHYSICAL JOURNAL SPECIAL TOPICS

Regular Article

Fractal dimension-based viability analysis of cancer cell lines in lens-free holographic microscopy via machine learning

Muhammed Ali Pala[1,a], Murat Erhan Çimen[1], Akif Akgül[2], Mustafa Zahid Yıldız[1], and Ali Fuat Boz[1]

[1] Department of Electrical and Electronics Engineering, Faculty of Technology, Sakarya University of Applied Sciences, Sakarya 54050, Turkey
[2] Department of Computer Engineering, Faculty of Engineering, Hitit University, Çorum 19030, Turkey

Received 30 June 2021 / Accepted 30 October 2021

Abstract Cell studies play an important role in the basis of studies on cancer diagnosis and treatment. Reliable viability assays on cancer cell studies are essential for the development of effective drugs. Lens-free digital in-line holographic microscopy has become a powerful tool in the characterization and viability analysis of microparticles such as cancer cells due to its advantages such as high efficiency, low cost, and flexibility to integrate with other components. This study is designed to perform viability tests using fractal dimensions of alive and dead cancer cells based on digital holographic microscopy and machine learning. In the in-line holography configuration, a microscopy assembly consisting of inexpensive components was built using an LED source, and the images were reconstructed using computational methods. The standard US Air Force Resolution Target was used to evaluate the capability of our imaging setup then holograms of stained cancer cells were recorded. To characterize individual cells, 19 different rotational invariant fractal dimension values were extracted from the images as features. An artificial neural network technique was employed for the classification of fractal features extracted from cells. The artificial neural network was compared with four other machine learning techniques through five different classification performance measures. The empirical results indicated that artificial neural networks performed better than compared classification techniques with accuracies of 99.65%. The method proposed in this paper provides a new method for the study of cell viability which has the advantages of high accuracy and potential for laboratory application.

1 Introduction

Cellular sensitivity, response and drug studies performed in-vitro in laboratory environments are the first step activities in achieving clinical success. Imaging and analyzing cells and micro-particles in laboratory environments and extracting meaningful relationships from the results are very important in the development of effective drugs and the conduct of clinical diagnosis and treatment processes [1]. In studies with cancer cell cultures, monitoring the population of cells and examining the cytotoxic effects of various drugs can be done by various methods. In current technological developments, viability analyzes are performed with cell analyzers, flow cytometry or optical microscopes [2,3]. These equipments consist of specialized optical components, taking into account the types of analysis to be performed. Analysis equipment has many disadvantages due to its low accuracy rate, high cost, bulky, specialized equipment, and the results cause expert-dependent subjective evaluations [4,5].

In recent years, the development of semiconductor sensor technologies at the micro-nano level has brought innovations in many fields. Digital in-line holographic microscopy (DIHM) technologies are one of the most important examples of these innovations that can be used in the medical field. DIHM is widely popular for its simple arrangement. DIHM can be used in the medical field for imaging and analysis of cancer cell lines, hemogram tests, urine tests, examining pathological samples, and determining the three-dimensional positions of microparticles [6–10]. DIHM systems are built with a light source and imaging sensor. Charge Coupled Device (CCD) or Complementary Metal-Oxide Semiconductor (CMOS) can be used as an imaging sensor. CMOS sensors are more commonly preferred due to the sensitivity, small pixel size and sensitivity they provide [11]. Laser, laser diode or light emitting diodes (LED) can be used as light sources. Laser sources are widely used due to their high temporal and spatial coherence. However, too high coherence can degrade the quality of the resulting images and cause speckle noise. LED light sources, on the other hand, are frequently used in the imaging of medical microparticles, because they do

[a] e-mail: pala@subu.edu.tr (corresponding author)

Published online: 26 November 2021

not cause these noises and are easy to operate [9,12]. The pinhole used with LED sources makes the incoherent source partially coherent and provides sufficient interference of the sample plane.

Cell viability assays are used to identify conditions that cause cell death as a result of the physical or chemical processes that cells are exposed to. Cells exposed to cytotoxic substances may die as a result of events, such as apoptosis, autophagy and necrosis, or the cell may lose its proliferation properties for various reasons [13]. Due to this situation, various morphological and functional changes occur in the structures of cells. To determine the viability with the help of chemicals, calorimetric, luminescence and enzymatic methods are preferred [14]. Staining with trypan blue, which is one of the chemical processes, is known as one of the most reliable methods in viability analysis [15]. There are many feature-based methods in the literature for the automated measurement and evaluation of cellular changes resulting from the application of these methods [16–19]. Feature extraction can be done over the amplitude and phase components of the images obtained from DIHM systems. Morphological or optical features, such as area, roundness, major axis, refractive index, absorption of holographically transformed cells can be used as cell fingerprints [20]. Obtained features can be classified using machine learning methods or statistical methods [21,22].

The study of the development of the proportions of details existing in nature or a designed structure can be explained as fractal dimension calculation. As the fractal dimension value of the shape increases, so do the details [23,24]. As the calculated fractal dimension approaches 1, it indicates that the shape of the object approaches Euclidean geometry and the structure is not fractal. In other words, the larger the value of the fractal dimension, the more developed the properties of the object at different scales [25–29]. Briefly, fractal dimension values provide a relationship between fractal continuity and information richness (depth and detail). If the detail and richness of the image are high, the fractal dimension value is also high. Therefore, the fractal dimension emerges as a function of the image. Using this function, fractal dimension values, which are the distinguishing features of the image, can be calculated and used as feature values. In this way, image recognition can be realized. Artificial neural networks, machine learning algorithms and deep neural networks are very powerful tools in the classification of features obtained from images.

In this study, a fractal dimension-based method is proposed that can perform viability analyzes of cancer cell lines with high accuracy and low loss rate. A microcomputer-based lens-free digital holographic microscopy setup was designed for imaging and viability analysis of cancer cell lines, and holograms of stained cancer cell cultures were collected. Captured holograms were numerically reconstructed, and amplitude images of cells were obtained. The US Air Force (USAF) target was used to evaluate the capability of our imaging setup and algorithms. The resulting images are divided into sub-images with the help of image processing algorithms. Individual cell images are labelled as live and dead. By rotating the cropped images at different angles, the angular independence of the features to be extracted is ensured. Fractal dimension calculations of all labelled cell images were made and 19 different features were calculated. Artificial neural network architecture is designed to classify using fractal features of cells. Artificial neural network architecture is designed to classify cells according to their calculated fractal features. The designed model was evaluated with various performance metrics and the results were compared with other machine learning algorithms frequently used in the literature. The artificial neural network model showed more success in many performance criteria compared to Random Forest, support vector machines, K-nearest neighbours and Decision Tree classifiers.

2 Materials and methods

2.1 Fractal

In Euclidean geometry, lines, circles, lines, polygons, cone-cylinders, and other forms with integer values of one, two, or three are shapes. With Euclidean geometry, it is often not possible to understand and mathematically express the complex structures that exist in nature. The concept of Fractal geometry was introduced by Mandelbrot to model shapes that do not fit Euclidean geometry. The term fractal is a word of Latin origin and means irregular, fragmented, divided and broken. Again, the term fractal is a general name given to complex or complex shapes that have the feature of resembling or repeating themselves in the field of mathematics. The term fractal is defined as a shape consisting of parts that resemble a whole. For this reason, the term fractal is the phenomenon of finding similar structures in the shape when looking at the overall shape. As a result, the parts that make up the shape in a fractal structure resemble each other and, therefore, the whole shape. These pieces can be thought of as replicas of the similarity. Although there are repetitive structures in fractal geometry, these structures can have a constantly growing or shrinking feature. In this case, the concept of fractal dimension comes into play. Each small piece is a copy or similar of the whole piece. The fractal dimension represents a measure of self-similarity.

Fractals can be formed by the repetition of geometries with similar shapes, or they can also be formed by the repetition of geometries with shapes that are not similar to themselves randomly. In this case, fractal structures are divided into different categories within themselves. Fractals are divided into three categories as self-similarity, semi-similarity and statistical similarity [30]. Fractal shapes with a geometric structure formed by random repetition are generally found in nature. However, according to Sertöz, there is a limit to these

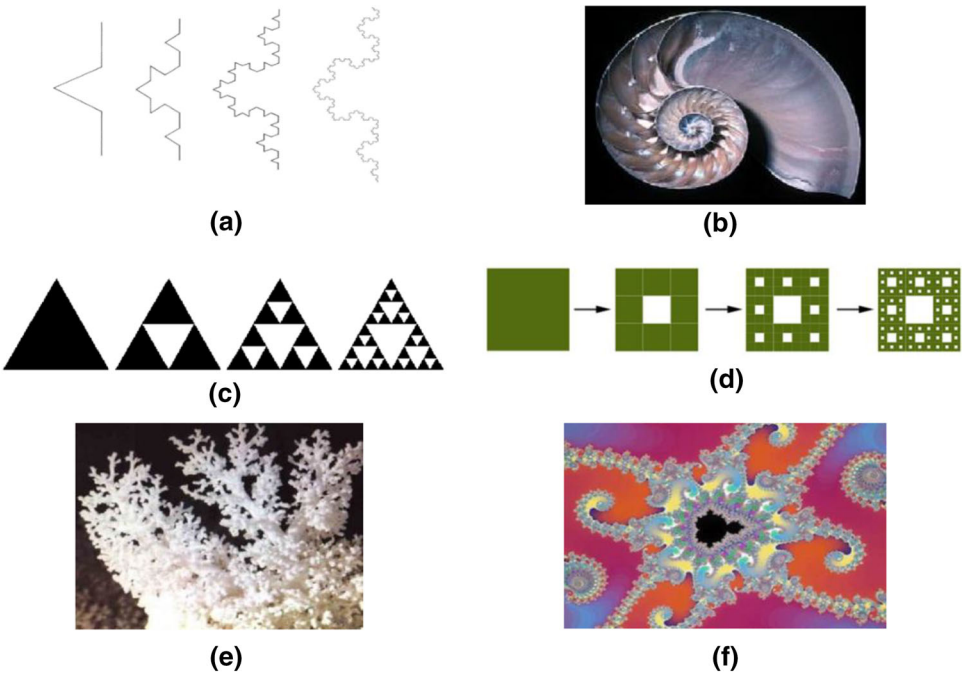

Fig. 1 Example fractal structures that can be encountered in nature or produced in computer environment, **a** Koch spline, **b** snail shell, **c** Sierpinski triangle, **d** Sierpinski carpet, **e** lung airways, **f** digitally created fractal structure

repetitions [31]. Some fractal images encountered in the literature are given in Fig. 1.

Fractal geometry is used in many fields from medicine, economy, biology, engineering, architecture, music, astronomy to geography, physics to art. Particularly, it can be noticed when looking carefully that an object consists of parts that are the same as a whole, or that the disorder of the whole is similar to the irregularity of the parts, which is encountered in many elements found in nature. For example, when the coastline of lands is examined, there are indentations and protrusions in any part of the coast, just as in the whole [32]. Such fractal structures are rivers, rivers, clouds, branching of trees, leaf patterns, snowflakes, capillaries, lung airways, fault lines, nerve fibres or tornado, etc. found in nature [24,33]. Considering the application areas, fractals are used in a wide range. Uyar et al. they used fractal geometry to study landforms [32]. Bayrak et al. performed fractal analysis on thyroid ultrasound images in their study [25]. Sezer et al. used fractal analysis to measure the strength of some materials [27].

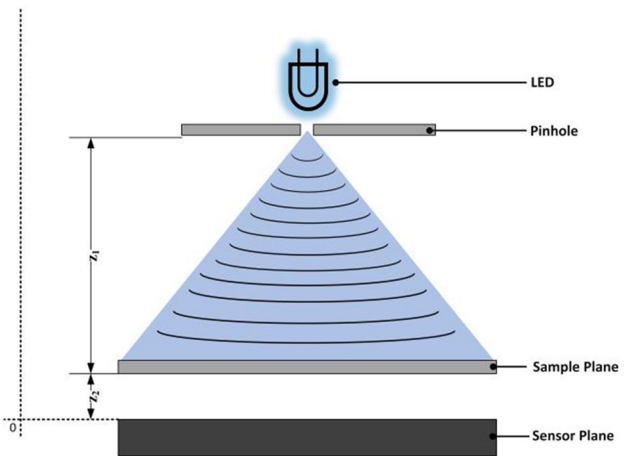

Fig. 2 Schemes of the digital in-line holographic microscope (DIHM)

2.2 System setup

A digital in-line holographic microscopy setup based on LED illumination and CMOS imaging sensor was built to capture holograms of cells. The experimental setup is shown in Fig. 2. The sample plane was illuminated by the LED light source and the interference pattern from the sample plane was captured by the CMOS sensor and the holograms were digitally recorded. LED sources are widely preferred in lens-free imaging systems due to their ease of use and cost. The used LED light source has a central wavelength of 405 nm. The spatial consistency of the light source is required to achieve interference. For this purpose, the LED light source is focused on a 300 µm pinhole. The use of pinhole in the setup makes the incoherent LED source to partially coherent and provides spatial filtering. The distance between the pinhole and sample (z_1) was fixed at approximately 60 mm. Sony IMX219PQ CMOS imaging sensor was used to capture holograms. The CMOS-sensor chip has a 3280 × 2464 pixel active area with 1.12 µm pixel size. The CMOS sensor was commercially available and easy to assemble and disassemble. Medical specimens are placed directly on the imaging sensor. The distance between the sample plane and the CMOS sensor (z_2) is less than 1 mm. Parameters such as the exposure time of the CMOS imaging sensor, ISO and white balance are manually adjusted. The PWM signal was controlled by

the microcomputer to synchronize the LED light source during the hologram capture. Since the CMOS imaging sensor has a BAYER filter, the captured holograms are RGB images and only the green channel is used in the recording processes. The recorded holographic images were transferred to the computer for reconstruction, fractal features extraction and classification.

2.3 Holography

The concept of holography was first proposed by Gabor. By definition, in-line holography is expressed as the sharing of the same optical axis between the waves of the object and the reference waves emitted from the light source [34]. Compared to methods, such as off-axis holography, in-line holography configurations can record the diffraction pattern with simpler experimental setups. In the holographic recording process, the complex amplitude of the diffraction pattern of the sample is recorded, in other words, the phase and amplitude information of the sample light wave is obtained simultaneously. Therefore, the holographic data contains all the information of the sample. The digital hologram can be recorded by photosensitive sensors, such as CMOS. In the hologram plane, the object wave and the reference wave produce an interference pattern ($|I(x,y)|^2$) with a two-dimensional intensity distribution:

$$|I(x,y)|^2 = |R+O|^2 = |R|^2 + |O|^2 + R^*O + O^*R \quad (1)$$

Here, R^2 is the reference wave, O^2 is the zero-order diffraction of the object and is negligibly small. R^*O is the real image, O^*R is the twin image, R^* and O^* represent complex conjugates of waves. The interference pattern should be normalized to eliminate the inhomogeneous light distribution, noise-like dust particles or sensor sensitivity caused by illumination on the sensor plane and other effects [35]. Normalization can also be done by dividing the interference pattern by the reference wave or by subtracting the image obtained without a sample between the sensor and the light source. In this study, the image obtained without the object was extracted from the hologram image. After the normalization process:

$$\frac{|I(x,y)|^2}{|R|^2} \cong 1 + \frac{R^*O + O^*R}{|R|^2} \quad (2)$$

The twin-image remaining in the equation as a result of the normalization process reduces the signal-to-noise ratio (SNR) in digital in-line holography and, therefore, negatively affects the quality of the obtained image. Many iterative or non-iterative methods have been proposed to overcome this problem [36,37]. All cell images obtained in this study contain twin-images. This effect was considered as background noise in fractal feature extraction and machine learning processes. Therefore, phase retrieval or twin-image elimination was not applied to the hologram obtained in the study.

2.4 Hologram reconstruction

The in-line hologram recorded by the CMOS sensor must be digitally processed by back-propagation of the optical field. There are many numerical methods for reconstructing the digital hologram [38]. These methods aim to solve the diffraction integral of the field propagation. The angular spectrum method, also known as the double Fourier transform method, is widely used in DIHM systems due to its small sensor-to-sample distance. Compared to other methods, the angular spectrum method can be calculated using the Fourier transform without using any approximation. The angular spectrum is advantageous in terms of straightforward processing path resulting in low computational load and short calculation time, high efficiency especially in the paraxial regime, high fidelity and good discretization. In our DIHM setup, we directly back propagate the image from the sensor plane to the object plane with the angular spectrum method. The propagation function:

$$H(f_x, f_y, z) = \begin{cases} \exp\left[iz\frac{2\pi}{\lambda}\cdot\sqrt{1-(\lambda f_x)^2-(\lambda f_y)^2}\right], & (\lambda f_x)^2+(\lambda f_x)^2 < 1, \\ 0, & \text{otherwise} \end{cases} \quad (3)$$

where $H(f_x, f_y, z)$ is the transfer function in the Fourier space, z is the propagation distance, λ is the wavelength of the light source, i is the complex number and (f_x, f_y) is the coordinates in the Fourier space. The generated transfer function is multiplied by the hologram data converted to Fourier space and then converted back to real space:

$$I(x,y,z_2) = \Im^{-1}\left\{\Im\left\{I(x,y,0)\right\} H(f_x, f_y, z_2)\right\} \quad (4)$$

Here, $I(x,y,z_2)$ is the back propagated field, $I(x,y,0)$ is the hologram at sensor plane, $H(f_x, f_y, z_2)$ is the transfer function at sample plane, $\Im$ and $\Im^{-1}$ denote the 2D-Fourier transform and its invers form, respectively. The resulting back propagated field contains phase and amplitude information. In this study, only amplitude images were used.

In some cases, the distance between the sensor and the sample (z_2) may not be known precisely. To solve this situation, there are many autofocus metrics with or without reference image in the literature [39]. In this study, to find the optimum focusing distance, the transfer function was solved numerically by looping at 1 μm intervals. The individual Tamura coefficients of the images multiplied by the transfer function were calculated and the maximum value was chosen as the best focusing distance. A positive USAF 1951 resolution target was used to demonstrate the capability of our DIHM setup and to determine its resolution. The normalized raw hologram was converted to grey level and then interpolated. Images of USAF 1951 resolution target are given in Fig. 3a, b. In Fig. 3c, pixel intensity profiles are given.

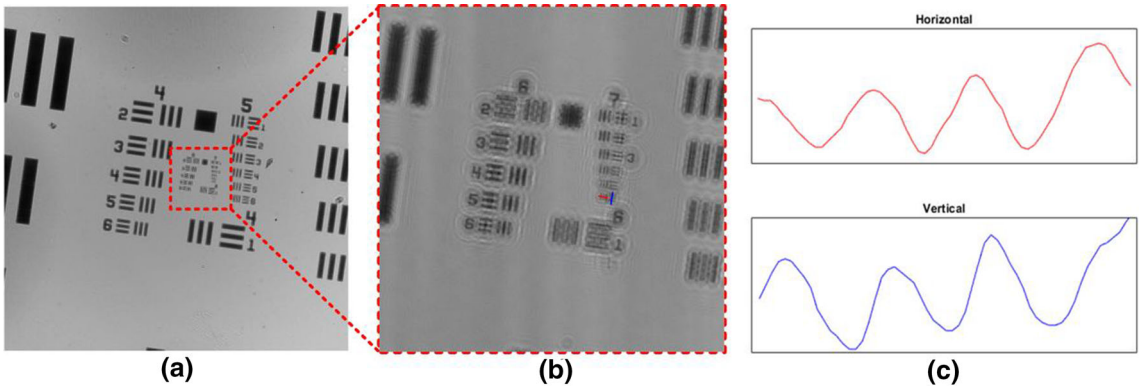

Fig. 3 Reconstruction of positive USAF 1951 resolution test target, **a** view of Group 4 and 5 of the raw hologram after normalization, **b** reconstructed image of ROI, **c** horizontal and vertical intensity profile through Element 6 of Group 7 (see colored bars in **b**)

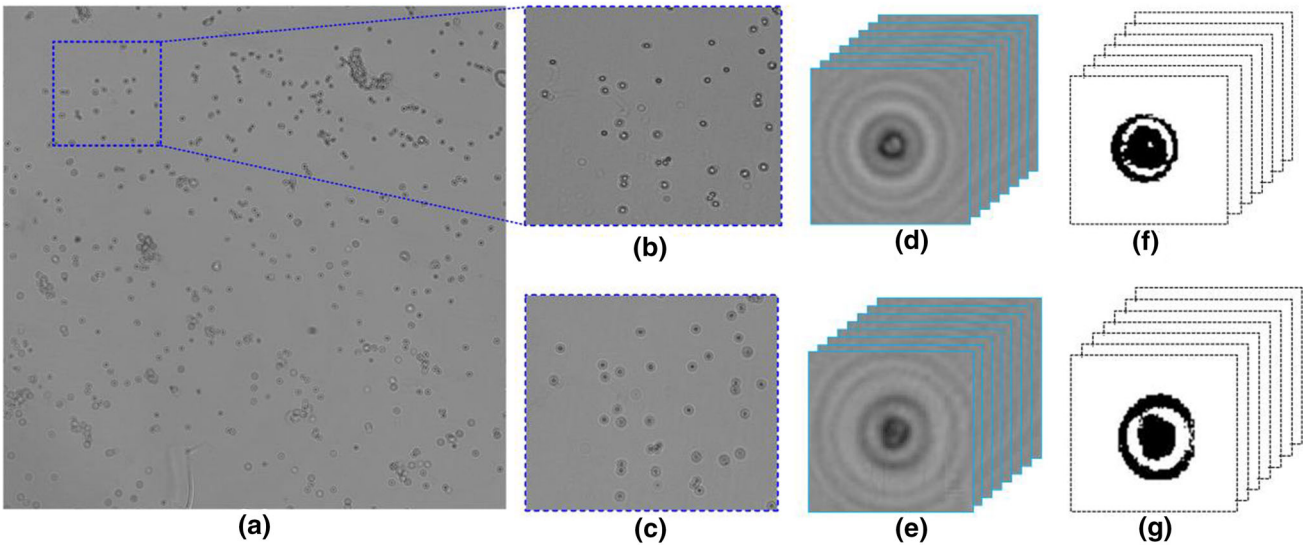

Fig. 4 Flow chart illustrating hologram reconstruction and data preparation, **a** raw hologram of cancer cells, **b** raw hologram of selected ROI, **c** reconstructed of **b**, **d** reconstructed alive cell, **e** reconstructed dead cells, **f** binary format of alive cell, **g** binary format of dead cell

3 Data collection

In this study, the MCF-7 cancer cell line, which is frequently used in the literature, was used to demonstrate the usability of fractal features in viability tests. MCF-7 cell line was supported with 10% fetal bovine serum and 1% penicillin and incubated at 37 °C with 5% CO_2. The cell line was transferred to ep-tubes and left at room temperature. These cell lines eventually died naturally over time. Cells were stained with trypan blue solution for viability analysis. Trypan blue was added to the cells in a ratio of 1:1 for 1 min. After injecting the 5 µL stained cells onto the glass, the chip was inserted into our DIHM setup.

Cells imaged with our DHM system were recorded as described above and reconstructed using the angular spectrum method. After reconstructing, the cells were individually sub-imaged to extract the fractal properties of each cell. In Fig. 4, cell images obtained with our DIHM system and data set preparation processes are given. To separate each cell individually from the whole sample image, all frame cell images were thresholded, binarized, holes filled, and finally, a morphological opening was applied. The centre of each cell was found in the binarized image and finally, we cropped individual holographic images of cells with a window of 250 × 250 pixels, as shown in Fig. 4d, e. The cropped grey level images were converted to black and white format by determining the adaptive threshold value for fractal feature extraction. 600 dead and 550 alive cells were identified on the reconstructed digital hologram and individually confirmed by researchers as ground truth. As a result, the data set contains a total of 1150 labelled cells.

4 Fractal dimension

The study of the development of the proportions of details existing in nature or in a designed structure can

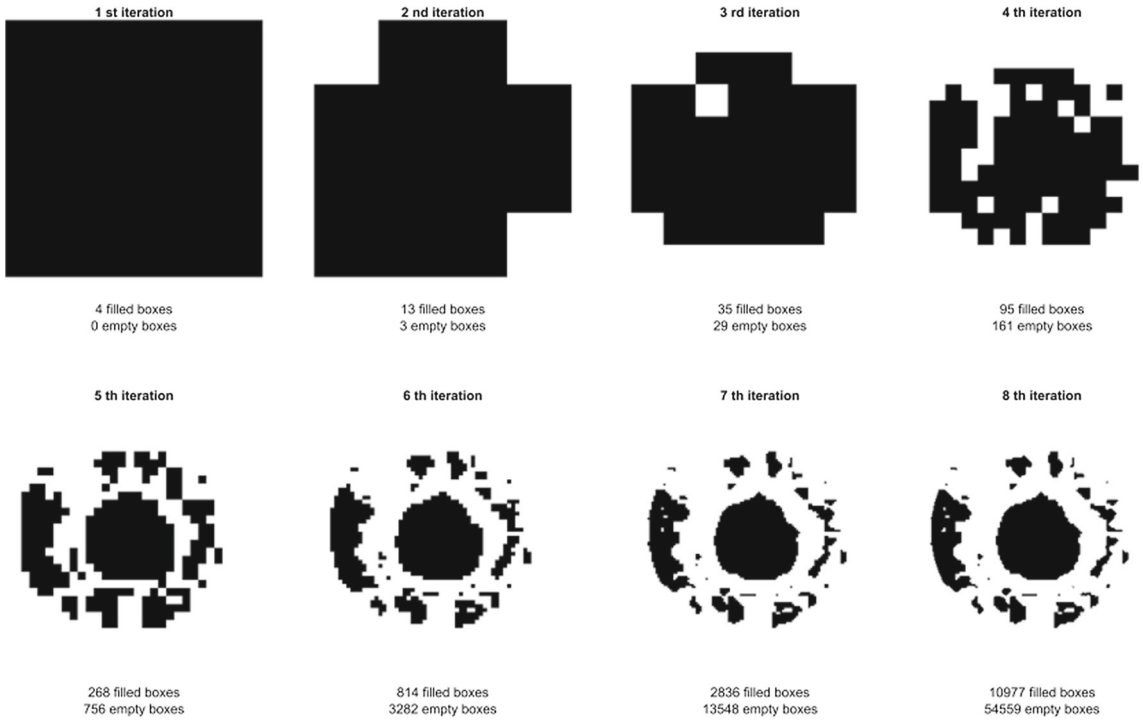

Fig. 5 Counting of full and empty boxes for fractal dimension calculation

Table 1 Number of full and empty boxes obtained by calculating the fractal dimension

	Filled boxes	Empty boxes
1th iteration	4	0
2nd iteration	13	3
3rd iteration	35	29
4th iteration	95	161
5th iteration	268	756
6th iteration	814	3282
7th iteration	2836	13,548
8th iteration	10,977	54,559

be explained as fractal dimension calculation. As the fractal dimension value of the shape increases, so do the details [23,24,28,29]. As the calculated fractal dimension approaches 1, it indicates that the shape of the object approaches Euclidean geometry and the structure is not fractal. In other words, the larger the value of the fractal dimension, the more developed the properties of the object at different scales [23–25]. Therefore, the fractal dimension emerges as a function of the image. The curling and box-counting methods are used to calculate the fractal dimension in the image. The curling method is a probability-based iterative process [40]. Since it depends on the probability of the coin, the resulting end continues until it reaches the equilibrium point. On the other hand, the box counting method is an iterative method based on counting the filled boxes on the image at different scales [30]. In the first iteration, the image is divided into segments and the filled boxes on the shapes are counted. In the 2nd iteration, the box size is reduced to 2 halves. The steps for each iteration are given in Fig. 5.

Filled boxes that fall on the shapes again are counted. Fractal dimensions are calculated using Eqs. (5) or (6). Briefly, fractal dimension values provide a relationship between fractal continuity and information richness (depth and detail). If the detail and richness of the image is high, the fractal dimension value is also high [29]. The results obtained are given in Table 1. In addition, fractal values calculated in each iteration using this value are given in Eq. (6):

$$D = \frac{\log\left(\begin{matrix}\text{filled boxes at}\\ \text{present iteration}\end{matrix}\right) - \left(\begin{matrix}\text{filled boxes at}\\ \text{previous iteration}\end{matrix}\right)}{\log\left(\begin{matrix}\text{sum of the all boxes at}\\ \text{present iteration}\end{matrix}\right) - \left(\begin{matrix}\text{sum of the all boxes at}\\ \text{previous iteration}\end{matrix}\right)} \quad (5)$$

$$D_{i+1,i} = \frac{\log\left(N_{i+1}\right) - \left(N_i\right)}{\log\left(2^{i+1}\right) - \left(2^i\right)} \quad (6)$$

$$D_{1,2} = \frac{\log\left(13\right) - \log(4)}{\log\left(4\right) - \log(2)} = 1.7004$$

$$D_{2,3} = \frac{\log\left(35\right) - \log(13)}{\log\left(16\right) - \log(4)} = 1.4288$$

$$D_{3,4} = \frac{\log\left(95\right) - \log(35)}{\log\left(64\right) - \log(16)} = 1.4406$$

$$D_{4,5} = \frac{\log\left(268\right) - \log(95)}{\log\left(128\right) - \log(64)} = 1.4962$$

$$D_{5,6} = \frac{\log\left(814\right) - \log(265)}{\log\left(256\right) - \log(128)} = 1.6028$$

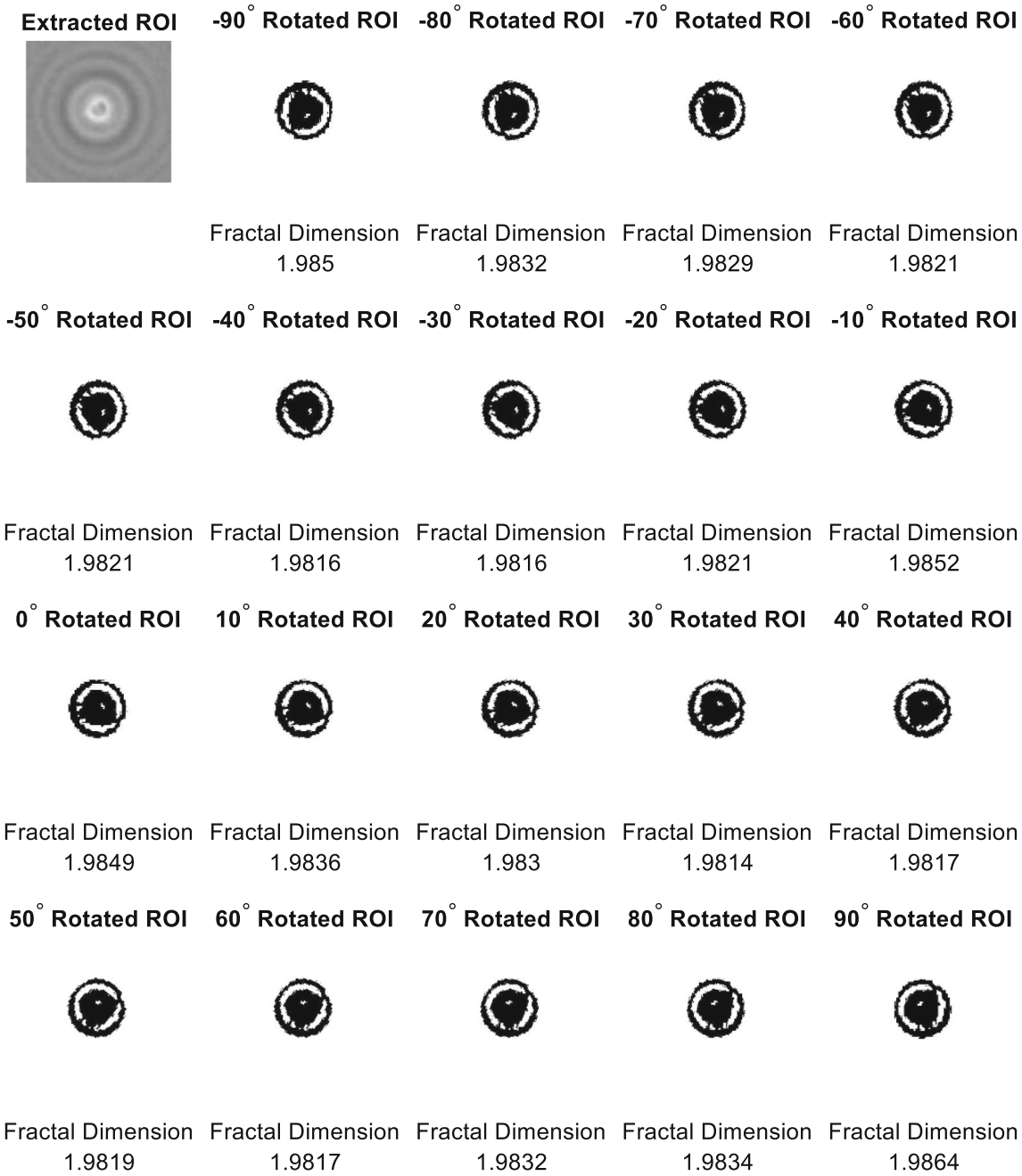

Fig. 6 Fractal values of the cell rotated and calculated at 10° intervals between −90° and 90°

$$D_{6,7} = \frac{\log(2836) - \log(814)}{\log(512) - \log(256)} = 1.8008$$
$$D_{7,8} = \frac{\log(10977) - \log(2836)}{\log(1024) - \log(512)} = 1.9526 \qquad (7)$$

In order for the obtained images to be independent of the angle, each image was rotated between −90° and 90° with 10° angles and their fractal values were calculated. The fractal values of a cell whose fractal value is calculated using this method are given in Fig. 6. The image taken from each cell was rotated at different angles in this way and 19 different fractal values were calculated. In addition, the data taken from each cell was shifted to increase the data. Therefore, 19 different fractal values were produced from 1 cell image. As an example, the expression of the data is given in Table 2. A total of 550 dead cells and 600 live cells were used. 21,850 number of data were produced with the data of these cells shifted at different angles. Moreover, using the obtained images, the different cells in the data set and their fractal values are briefly shown in Fig. 7.

4.1 Classification

Artificial neural networks are mathematical models inspired by the structure and functions of biological

Table 2 Fractal values of cells used and prepared in the data set

	Number of data							
	1	2	3	...	19	20	...	21,850
	Subjects							
	1					2	...	1150
Angle								
−90°	**1.985**	1.9864	1.9834	...	1.9832	1.9691		1.9693
−80°	1.9832	**1.985**	1.9864	...	1.9829	1.9653		1.9687
−70°	1.9829	1.9832	**1.985**	...	1.9821	1.9619		1.9785
−60°	1.9821	1.9829	1.9832	...	1.9821	1.9575		1.9678
−50°	1.9821	1.9821	1.9829	...	1.9816	1.9652		1.9659
−40°	1.9816	1.9821	1.9821	...	1.9816	1.9596		1.9729
−30°	1.9816	1.9816	1.9821	...	1.9821	1.9595		1.9721
−20°	1.9821	1.9816	1.9816	...	1.9852	1.9655		1.9731
−10°	1.9852	1.9821	1.9816	...	1.9849	1.9634		1.9742
0°	1.9849	1.9852	1.9821	...	1.9836	1.9688		1.9709
10°	1.9836	1.9849	1.9852	...	1.983	1.9653		1.9729
20°	1.983	1.9836	1.9849	...	1.9814	1.9612		1.9773
30°	1.9814	1.983	1.9836	...	1.9817	1.9590		1.9674
40°	1.9817	1.9814	1.983	....	1.9819	1.9646		1.9654
50°	1.9819	1.9817	1.9814	...	1.9817	1.9611		1.9708
60°	1.9817	1.9819	1.9817	...	1.9832	1.9622		1.9734
70°	1.9832	1.9817	1.9819	...	1.9834	1.9642		1.9761
80°	1.9834	1.9832	1.9817	...	1.9864	1.9624		1.9709
90°	1.9864	1.9834	1.9832	...	**1.985**	1.9696		1.9693

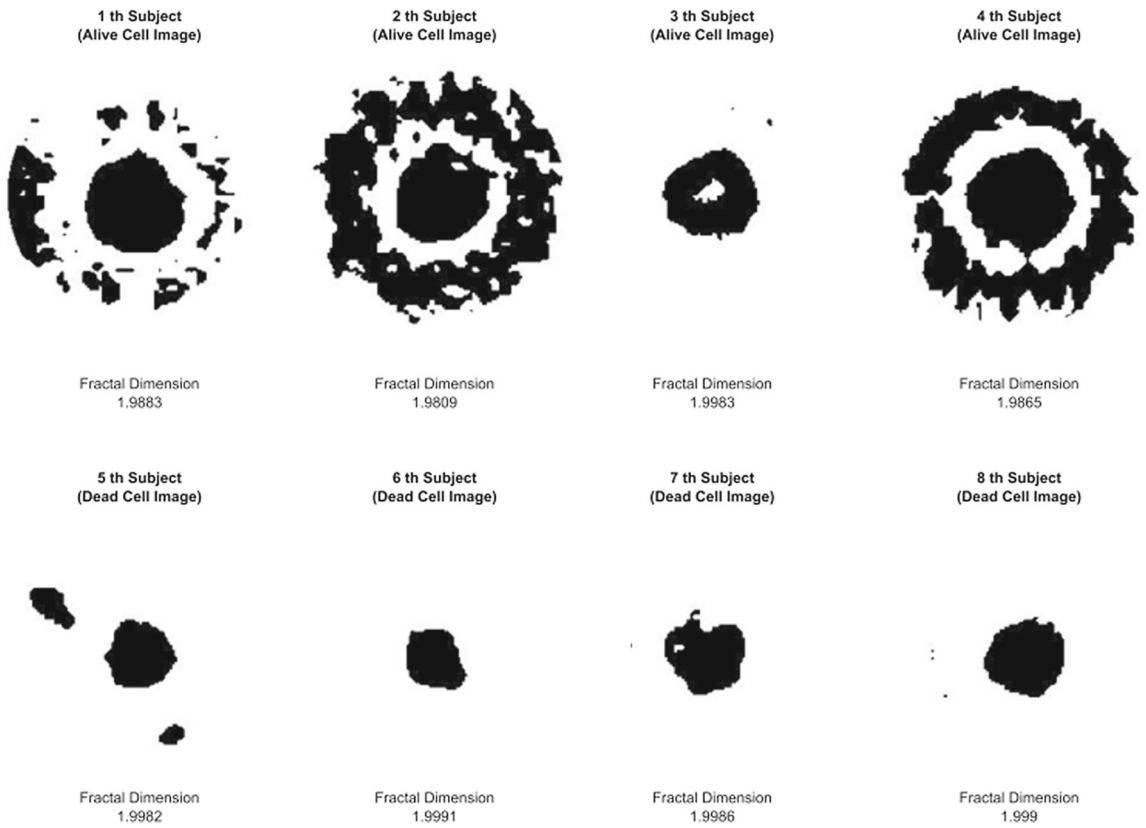

Fig. 7 Binary image and fractal values of randomly selected cells

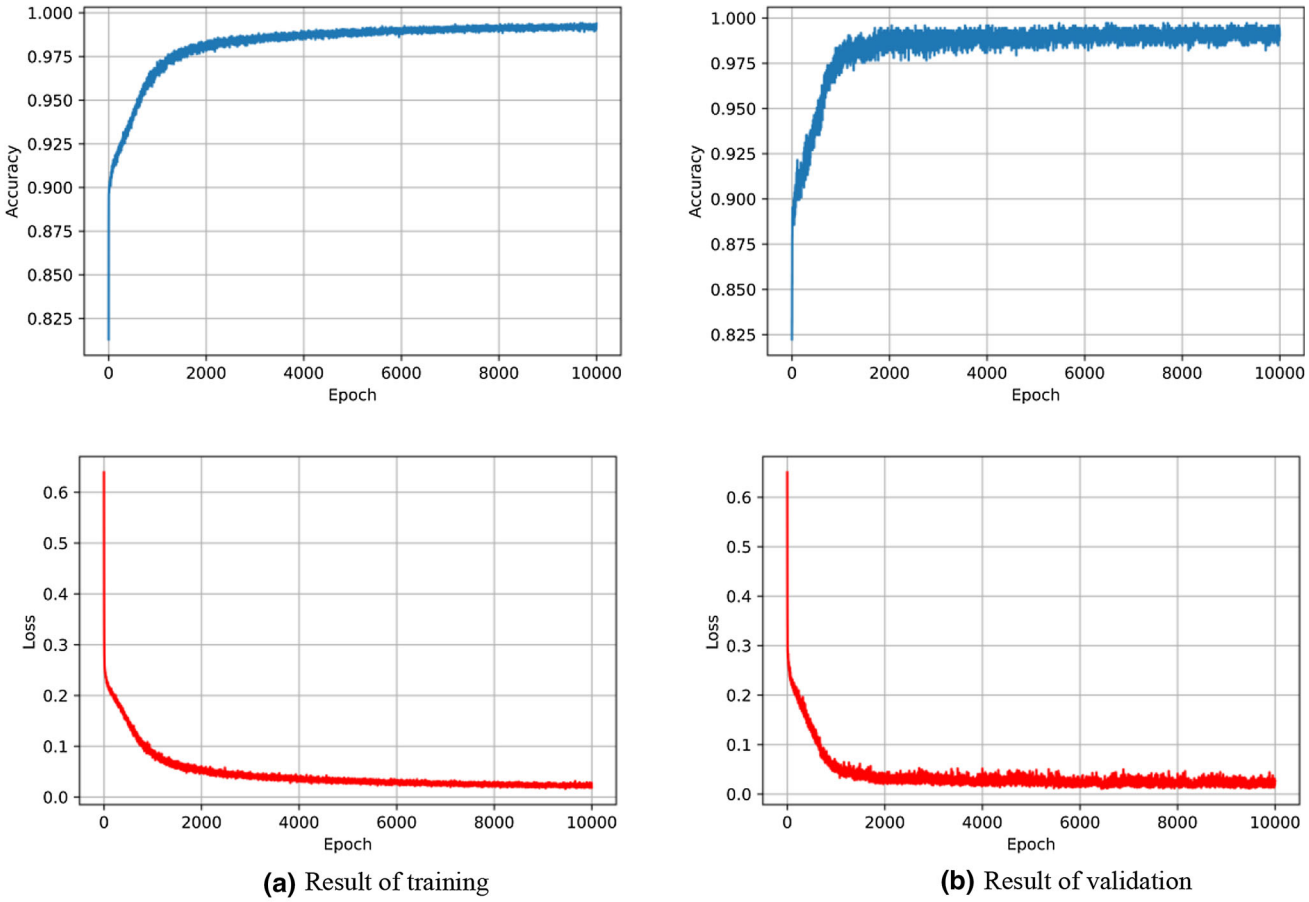

Fig. 8 Details of training and validation ANN, **a** graph of training accuracy and training loss during training of network, **b** graph of validation accuracy and validation loss during validating of network

neural networks, which can learn and test with data. Artificial neural networks are implemented in layers of non-linear feature operations, which consist of heavily interconnected processing units. As a basic rule multiplication, addition and activation functions they perform. The values taken as input are multiplied by a certain weight value, all obtained values are summed with the bias term and an activation operation is applied in the output layer. Today, artificial neural networks have many application areas. Especially in the medical field, it is frequently used for classification, pattern recognition, data mining, prediction and modelling [41–46]. It offers advantages such as being able to learn many linear or non-linear inputs quickly with high performance criteria and making stable generalizations. There are many artificial neural network architectures in the literature to fulfil various tasks [36]. It can be adapted to perform given tasks, such as classification, by changing the hyper-parameters contained in its architectural structures. In this study, an artificial neural network model was designed to maximize classification performance. The results obtained were compared with the machine learning methods frequently used in the literature. The classification performances of the features are shown with various performance analyzes.

Training and validation are important tasks in ANN applications. For this purpose, the data is divided into two parts as train and validation data. For this purpose, tenfold cross-validation methodology is applied to the data set to split data into training and validation. For the ANN classifier model, we used the back-propagation algorithm with a multi-layer perceptron (MLP). Relu activation function is used in the input and hidden layers. In order to stabilize the learning steps, a batch normalization layer was added to the output of each hidden layer. We used dropout of 0.1 after the hidden layers to avoid overfitting. The sigmoid is used as the activation function in the output layer. To optimize the weights, the training were made in 300 batch sizes and 10,000 epochs. Figure 8 shows the accuracy and loss graphs of the training and validation processes.

Other classification methods were also used to show the success of fractal features and to compare the success of the designed ANN architecture. Random Forest, support vector machine, K-nearest neighbours ($k = 10$) and Decision Tree classifiers were trained and tested with the same data set. Classification results were evaluated with frequently used performance criteria, such as Precision, Recall, F1-score, Accuracy, AUC (area under the ROC Curve). In Table 3, the average performance

Table 3 Classification performance measurements of machine learning algorithm

Classifier	Accuracy (%)	Precision	Recall	F1-score	AUC
Random Forest	90.77	0.91	0.89	0.90	0.88
Support vector machines	87.60	0.87	0.85	0.86	0.85
K-nearest neighbours	89.39	0.90	0.87	0.88	0.87
Decision Tree	87.05	0.86	0.85	0.86	0.85
ANN	99.65	0.99	0.98	0.98	0.98

values obtained as a result of the validation process are given.

Table 3 shows that Random Forest has an accuracy of 90.77%, support vector machines of 87.60%, K-nearest neighbours of 89.39%, Decision Tree of 87.05% and ANN of 99.65%. In addition, other performance criteria show parallel results with accuracy criteria. This suggests that the proposed ANN model has a clearly better classification performance for cells via fractal dimension. The ANN classifier appears to be more successful in classifying fractal dimension than other machine learning algorithms.

5 Conclusion

Cancer cell line studies play an important role in the clinical diagnosis, treatment and development of effective drugs. The novelty of this study is the angle-invariant fractal dimension analysis of the captured holographic images and the classification of cell viability using deep learning. Cell diffraction patterns were recorded with a low-cost, simple, easy-to-use LED light source-based DIHM experimental setup. The diffraction patterns were reconstructed using the angular spectrum method and the capability of the experimental microscopy setup was demonstrated with a standard USAF 1951 test target. 1150 cell images were recorded and then individually labelled by researchers as ground truth. The fractal dimension of each labelled image was calculated at 19 different angles. Cells were classified using these fractal features using ANN, Random Forest, support vector machine, K-nearest neighbours and Decision Tree machine learning algorithms. Classifier performances are measured using accuracy, precision, recall, F1-score and AUC metrics. Validation of results has been carried out by tenfold cross-validation. The highest classification accuracy of 99.65% was achieved using ANN. In addition, the designed ANN model showed higher performance in all measured metrics compared to other machine learning algorithms. In the proposed method, fractal features were shown to be like a fingerprint in cell viability analyzes and it was seen that they gave reliable results in cell viability analyses. The presented method can be utilized in a wide range of laboratory applications in cancer research.

Acknowledgements This work was supported by Sakarya University of Applied Science Scientific Research Projects Coordination Unit (SUBU BAPK, Project Number: 2020-01-01-011). The author, Muhammed Ali PALA, is grateful to The Scientific and Technological Research Council of Turkey for granting a scholarship (TUBITAK, 2211-C) for him Ph.D. studies.

References

1. M. Wei et al., An evaluation approach of cell viability based on cell detachment assay in a single-channel integrated microfluidic chip. ACS Sens. **4**(10), 2654–2661 (2019). https://doi.org/10.1021/acssensors.9b01061
2. K. Yang, J. Wu, S. Santos, Y. Liu, L. Zhu, F. Lin, Recent development of portable imaging platforms for cell-based assays. Biosens. Bioelectron. **124–125**(October 2018), 150–160 (2019). https://doi.org/10.1016/j.bios.2018.10.024
3. J. Sun, A. Tárnok, X. Su, Deep learning-based single-cell optical image studies. Cytom. Part A **97**(3), 226–240 (2020). https://doi.org/10.1002/cyto.a.23973
4. Y. Wu, A. Ozcan, Lensless digital holographic microscopy and its applications in biomedicine and environmental monitoring. Methods **136**, 4–16 (2018). https://doi.org/10.1016/j.ymeth.2017.08.013
5. M. Sher, R. Zhuang, U. Demirci, W. Asghar, Paper-based analytical devices for clinical diagnosis: recent advances in the fabrication techniques and sensing mechanisms. Expert Rev. Mol. Diagn. **17**(4), 351–366 (2017). https://doi.org/10.1080/14737159.2017.1285228
6. J. Li, L. Dai, N. Yu, Z. Li, S. Li, Measurement of red blood cell size based on a lensless imaging system. Biotechnol. Appl. Biochem. (2020). https://doi.org/10.1002/bab.2057
7. J. Kun, M. Smieja, B. Xiong, L. Soleymani, Q. Fang, The use of motion analysis as particle biomarkers in lensless optofluidic projection imaging for point of care urine analysis. Sci. Rep. **9**(1), 17255 (2019). https://doi.org/10.1038/s41598-019-53477-8
8. J. Mariën, R. Stahl, A. Lambrechts, C. van Hoof, A. Yurt, Color lens-free imaging using multi-wavelength illumination based phase retrieval. Opt. Express **28**(22), 33002 (2020). https://doi.org/10.1364/oe.402293
9. A.B. Dharmawan et al., Nonmechanical parfocal and autofocus features based on wave propagation distribution in lensfree holographic microscopy. Sci. Rep. **11**(1), 3213 (2021). https://doi.org/10.1038/s41598-021-81098-7

10. M. Rempfler et al., Tracing cell lineages in videos of lens-free microscopy. Med. Image Anal. **48**, 147–161 (2018). https://doi.org/10.1016/j.media.2018.05.009
11. M. Roy, D. Seo, S. Oh, J.W. Yang, S. Seo, A review of recent progress in lens-free imaging and sensing. Biosens. Bioelectron. **88**, 130–143 (2017). https://doi.org/10.1016/j.bios.2016.07.115
12. G. Scholz et al., Continuous live-cell culture imaging and single-cell tracking by computational lensfree LED microscopy. Sensors (Switzerland) **19**(5), 1–13 (2019). https://doi.org/10.3390/s19051234
13. Z. El-Schich, A. Mölder, H. Tassidis, P. Härkönen, M.F. Miniotis, A.G. Wingren, Induction of morphological changes in death-induced cancer cells monitored by holographic microscopy. J. Struct. Biol. **189**(3), 207–212 (2015). https://doi.org/10.1016/j.jsb.2015.01.010
14. K. Yamashita, R. Tagawa, Y. Higami, E. Tokunaga, Noninvasive and safe cell viability assay for breast cancer MCF-7 cells using natural food pigment. Biology (Basel) **9**(8), 1–14 (2020). https://doi.org/10.3390/biology9080227
15. F. Piccinini, A. Tesei, C. Arienti, A. Bevilacqua, Cell counting and viability assessment of 2D and 3D cell cultures: expected reliability of the trypan blue assay. Biol. Proc. Online **19**(1), 1–12 (2017). https://doi.org/10.1186/s12575-017-0056-3
16. M.A. Pala, M.E. Çimen, Ö.F. Boyraz, M.Z. Yildiz, A.F. Boz, Meme Kanserinin Teşhis Edilmesinde Karar AğacıVe KNN Algoritmalarının KarşılaştırmalıBaşarım Analizi. Acad. Perspect. Procedia **2**(3), 544–552 (2019). https://doi.org/10.33793/acperpro.02.03.47
17. T. O'Connor, A. Anand, B. Andemariam, B. Javidi, Overview of cell motility-based sickle cell disease diagnostic system in shearing digital holographic microscopy. J. Phys. Photon. (2020). https://doi.org/10.1088/2515-7647/ab8a58
18. D. De Bels et al., Hyperoxia alters ultrastructure and induces apoptosis in leukemia cell lines. Biomolecules **10**(2), 1–14 (2020). https://doi.org/10.3390/biom10020282
19. Ö.F. Boyraz, M.A. Pala, M.E. Çimen, Mikrobilgisayar TabanlıEl- Bilek Damar Örüntüleri Kullanılarak Biyometrik Kimlik Doğrulama İşleminin YapılmasıA microcomputer-based biometric authentication system using hand-wrist vein patterns. 2019(November), 593–600 (2019)
20. C.L. Chen et al., Deep learning in label-free cell classification. Sci. Rep. **6**(March), 1–16 (2016). https://doi.org/10.1038/srep21471
21. A. Caliskan, M.E. Yuksel, H. Badem, A. Basturk, Performance improvement of deep neural network classifiers by a simple training strategy. Eng. Appl. Artif. Intell. **67**, 14–23 (2018). https://doi.org/10.1016/j.engappai.2017.09.002
22. Y. Wang, P. Ju, S. Wang, J. Su, W. Zhai, C. Wu, Identification of living and dead microalgae cells with digital holography and verified in the East China Sea. Mar. Pollut. Bull. **163**(December 2020), 111927 (2021). https://doi.org/10.1016/j.marpolbul.2020.111927
23. B. Klinkenberg, A review of methods used to determine the fractal dimension of linear features. Math. Geol. **26**(1), 23–46 (1994)
24. A.O. Öncel, Ö. Alptekin, Fraktal dağılım ve sismolojideki uygulamaları. Jeofizik Derg. **9**(1) (1995)
25. P. Kirci, E.A. Bayrak, The application of fractal analysis on thyroid ultrasound images. Acta Infologica **3**(2), 89–90 (2019)
26. L. Yu, D. Zhang, K. Wang, W. Yang, Coarse iris classification using box-counting to estimate fractal dimensions. Pattern Recognit. **98**(11), 1791–1798 (2005)
27. A. Sezer, A.B. Göktepe, S. Altun, Temel dayanımının fraktal boyut ile incelenmesi (2007)
28. M.E. Çimen, Ö.F. Boyraz, Z. Garip, İ. Pehlivan, M.Z. Yildiz, A.F. Boz. Görüntü İşleme Tabanlı Kutu Sayma Yöntemi ile Fraktal Boyut Hesabı için Arayüz Tasarımı. Politek. Derg. **24**(3), 867–878 (2021). https://doi.org/10.2339/politeknik.689421
29. M.E. Cimen, O.F. Boyraz, M.Z. Yildiz, A.F. Boz, A new dorsal hand vein authentication system based on fractal dimension box counting method. Optik. **226**, 165438 (2021)
30. A.K. Bisoi, J. Mishra, On calculation of fractal dimension of images. Pattern Recognit. Lett. **22**(6–7), 631–637 (2001). https://doi.org/10.1016/S0167-8655(00)00132-X
31. E. Demireli, M. Ural, Hurst Üstel katsayisi araciliğiyla fraktal yapi analizi ve İMKB'de bir uygulama. Atatürk. Üniversitesi İktisadi ve İdari Bilim. Derg. **23**(2), 243–255 (2009)
32. A. Uyar, D. Öztürk, Fraktal analizin yeryüzü araştırmalarında kullanılması. Afyon Kocatepe Üniversitesi Fen ve Mühendislik Bilim. Derg. **17**(4), 147–155 (2017)
33. Q. Huang, J.R. Lorch, R.C. Dubes, Can the fractal dimension of images be measured? Pattern Recognit. **27**(3), 339–349 (1994). https://doi.org/10.1016/0031-3203(94)90112-0
34. D.G. Voelz, *Computational Fourier optics: a MATLAB Tutorial* (SPIE Press, Bellingham, 2011), pp. 116–124
35. T. Latychevskaia, H.W. Fink, Practical algorithms for simulation and reconstruction of digital in-line holograms. Appl. Opt. **54**(9), 2424–2434 (2015). https://doi.org/10.1364/AO.54.002424
36. Z. Ren, Z. Xu, E.Y. Lam, End-to-end deep learning framework for digital holographic reconstruction. Adv. Photon. **1**(01), 1 (2019). https://doi.org/10.1117/1.ap.1.1.016004
37. L. Hervé et al., Alternation of inverse problem approach and deep learning for lens-free microscopy image reconstruction. Sci. Rep. **10**(1), 1–12 (2020). https://doi.org/10.1038/s41598-020-76411-9
38. S. Feng, J. Wu, Differential holographic reconstruction for lensless in-line holographic microscope with ultra-broadband light source illumination. Opt. Commun. **430**(August 2018), 9–13 (2019). https://doi.org/10.1016/j.optcom.2018.08.033
39. H.A. Ilhan, M. Dogar, M. Ozcan, Digital holographic microscopy and focusing methods based on image sharpness. J. Microsc. **255**(3), 138–149 (2014). https://doi.org/10.1111/jmi.12144
40. A. Bigerelle, Maxence; IOST, "Fractal dimension and classification of music". Chaos Solitons Fractals **11**(14), 2179–2192 (2000)
41. S.H. Rezatofighi, H. Soltanian-Zadeh, Automatic recognition of five types of white blood cells in periph-

eral blood. Comput. Med. Imaging Graph. **35**(4), 333–343 (2011). https://doi.org/10.1016/j.compmedimag.2011.01.003
42. M. E. Çimen, Z. Garip Batık, M. A. Pala, B. A. Fuat, A. Akgul, Modelling of chaotic motion video with artificial neural networks. Chaos Theory Appl. **1**(1), 38–50 (2019)
43. K. Kourou, T.P. Exarchos, K.P. Exarchos, M.V. Karamouzis, D.I. Fotiadis, Machine learning applications in cancer prognosis and prediction. Comput. Struct. Biotechnol. J. **13**, 8–17 (2015). https://doi.org/10.1016/j.csbj.2014.11.005
44. M. Alcin, I. Koyuncu, M. Tuna, M. Varan, I. Pehlivan, A novel high speed artificial neural network-based chaotic true random number generator on field programmable gate array. Int. J. Circuit Theory Appl. **47**(3), 365–378 (2019). https://doi.org/10.1002/CTA.2581
45. M. Tuna, A. Karthikeyan, K. Rajagopal, M. Alcin, İ Koyuncu, Hyperjerk multiscroll oscillators with megastability: analysis, FPGA implementation and a novel ANN-ring-based true random number generator. AEU Int. J. Electron. Commun. **112**, 152941 (2019). https://doi.org/10.1016/J.AEUE.2019.152941
46. S. Vaidyanathan et al., A novel ANN-based four-dimensional two-disk hyperchaotic dynamical system, bifurcation analysis, circuit realisation and FPGA-based TRNG implementation. Int. J. Comput. Appl. Technol. **62**(1), 20–35 (2020). https://doi.org/10.1504/IJCAT.2020.103921